

Infrared Space Observatories: How to Mitigate Zodiacal Dust Interference

P. Gurfil¹, J. Kasdin¹, R. Arrell¹, S. Seager², S. M. Nissanke³

ABSTRACT

Out-of-the-ecliptic trajectories that are beneficial to space observatories such as the Terrestrial Planet Finder and other potential mid-IR missions are introduced. These novel trajectories result in significantly reduced background noise from the zodiacal dust radiation and therefore allow a reduction in the necessary size of the telescope collecting area. The reduced size of the mirrors allows for a considerable reduction in payload mass and manufacturing costs. Two types of optimal trajectories that are energetically feasible were derived using genetic algorithms. These are highly inclined non-Keplerian heliocentric orbits.

We use the zodiacal dust model from the COBE data to determine how well the orbits mitigate the interference from the zodiacal dust. The first optimal trajectory can use existing launch technology and yields a maximum decrease of 67% in the zodiacal cloud brightness. The zodiacal brightness for this trajectory is reduced by at least 50% for 60% of the mission lifetime. The second optimal trajectory requires planned improvement in launch technology but it renders a dramatic 97% maximum noise decrease. The zodiacal cloud brightness is reduced by at least 70% for 82% of the mission lifetime for this trajectory.

Heliocentric orbits at 5 AU have been discussed because the zodiacal dust concentration is extremely low there and the energy requirements to reach these trajectories are low if gravitational assists can be used. Unfortunately such orbits are impractical because of high cost, power source constraints (inability to use solar cells), communication delays, and a long travel time before data return. Additionally, the energy requirements to reach the low and high energy trajectories are respectively half as much and equivalent to a direct trip to 5AU with no planetary gravitational assists.

1. Introduction

An unprecedented interest in space-borne observation missions has arisen out of NASA's Origins Program, a collection of missions aimed at determining and characterizing the origin and development of galaxies, stars, planets, and the chemical conditions necessary to support extraterrestrial life⁴. Over the course of the next two decades, the Origins Program will focus on developing space-based observatories through a series of precursor missions such as the Space Infrared Telescope Facility (SIRTF); first generation missions, such as Space Technology 3 (ST3), Space Interferometry Mission (SIM) and the Next Generation Space Telescope (NGST); and second generation missions, such as the Terrestrial Planet Finder (TPF).

One of the most important constraints of such missions is the so-called zodiacal dust (zodi) or interplanetary dust. In our own solar system, dust (very tiny solid particles composed of silicates, ices,

¹Dept. of Mechanical and Aerospace Engineering, Princeton University, Princeton, NJ, USA

²Institute for Advanced Study, Einstein Drive, Princeton, NJ, USA

³Department of Physics, Cambridge University, Cambridge, UK

⁴<http://origins.jpl.nasa.gov>

and other minerals) is ever present. This material is both a remnant of the formation of the planets and a consequence of continuing collisions among comets, asteroids, and other small bodies. The zodi has a potentially serious impact on the ability of space-borne observatories to detect and study their targets. Specifically, the zodi reveals itself as a diffuse component of the sky brightness, attributed to the scattering of sunlight in the UV, optical, and near-IR, and the thermal re-radiation of absorbed energy in the mid-IR and far-IR. At infrared wavelengths from approximately $1 \mu\text{m}$, the signal from the zodi is a major contributor to the diffuse sky brightness and dominates the mid-IR ($10\text{--}60 \mu\text{m}$) sky in nearly all directions (except very low galactic latitudes). Consequently, the emission from the local zodi is a major noise source, considerably affecting the size and weight requirements of the mirrors. In Beichman, Woolf, & Lindensmith (1999) it is shown that for a 1 AU TPF mid-IR interferometer mission, the local zodiacal background constitutes roughly 70% of the total noise. The intensity of the zodi radiation (in terms of thermal emission) is greatly reduced when moving in a direction normal to the ecliptic plane.

The zodiacal dust problem is the principal motivation for the design of trajectories having considerable displacements normal to the ecliptic. We have examined a widely used zodi model that was measured by the Cosmic Background Explorer (COBE) and the Infrared Astronomical Satellite (IRAS) (Kelsall et al. 1998). Simulation of this model quantifies the evolution of the zodi brightness (from thermal emission only) as a function of the height above the ecliptic plane, at various Earth positions. The results are depicted in Figure 1, with λ denoting Earth's angular position relative to the Sun. It is apparent that at 0.18 AU above the ecliptic plane more than 50% of the emission is avoided, and at 0.4 AU above the ecliptic, more than 80% of the emission is avoided. While higher excursions reduce further the noise generated by the zodi emission, the energetic requirements involved may be substantial. In other words, the 0.4 AU point on the abscissa of Figure 1 represents a threshold above which the dependence of the normalized brightness on the height above the ecliptic plane is small when compared to the energy cost to get there.

A variety of orbits have been considered for other missions. The diversity of these missions and their stringent resolution and accuracy requirements necessitates the design of specialized trajectories. For example, for the NGST mission, a halo orbit around the collinear Lagrangian libration point has been considered (Lubow 2000). For the TPF and Darwin missions, orbits at 5 AU where the zodi is highly reduced are being considered (Landgraf & Jehn 2001) but cost, communication, power, and delay to data return can be problematic. For the TPF mission, both L_2 and heliocentric Earth-trailing orbits have also been examined (Beichman et al. 1999). To date, several types of trajectories associated with the collinear libration points have been reported. These trajectories are obtained by exploring either the planar circular restricted three-body problem (CR3BP) or the spatial CR3BP. The so-called Lyapunov orbits obtained in the planar case (Szebehely 1967) bifurcate into a spatial family of Lissajous orbits (Gomez, Massdemont, & Simo 1997), which generate the well-known Halo orbits as a particular case only when perturbations are ignored and specific initial conditions are selected (Howell, Barden, & Lo. 1997; Henon 1974; Goudas 1963). While libration point orbits have been widely explored — as they often offer valuable operational and scientific features — less attention has been given to other trajectories emerging from the spatial CR3BP that are more suitable for the unique constraints of mid-IR space-borne observation missions.

This paper describes work aimed at synthesizing families of out-of-the-ecliptic trajectories, which mitigate the effects of the zodi. In §2 we discuss the zodiacal dust model, in §3 we describe the optimal trajectories, and §4 follows with a summary and discussion.

2. The Local Zodiacal Cloud Model

The scattered light and thermal emission from the zodiacal dust cloud within our own solar system contribute significantly to the diffuse sky brightness observable at most infrared wavelengths. The zodi has been investigated extensively using observations from the IRAS satellite and the most recent detailed COBE Diffuse Infrared Background Experiment (DIRBE). A model of the zodi was used to evaluate the effectiveness of the orbits described in this paper. The parameterized physical model of the zodi that was used is a simplified version of the highly complex model developed in direct conjunction with the measurements from the COBE DIRBE satellite (Kelsall et al. 1998).

As the following equation and discussion demonstrate, the model brightness is calculated as the integral of the product of a source function and a three-dimensional dust density distribution function evaluated along the line of sight,

$$I_\nu = \int E_{c,\nu} B_\nu(T(R)) n_c(X, Y, Z) ds. \quad (1)$$

At infrared wavelengths of approximately 10-60 μm , thermal reradiation of absorbed energy from the zodi is estimated to contribute 90% or more to the total sky brightness in nearly all directions (except at very low Galactic latitudes). In contrast, the scattered sunlight contribution is of significance in the UV, optical, and near-IR. Therefore, as a first approximation, it can be neglected in the case of an observing mission centered at a 12 μm wavelength. The simplified model thus considers the thermal emission contribution of the zodi, which is expressed in equation (1) as a blackbody $B_\nu(T(R))$, and its associated emissivity modification factor at 12 μm $E_{c,\nu}$ (initially a free parameter in the original DIRBE model) which is $E_{c,12\mu\text{m}} = 0.958$. The dust grain temperature T variation with distance from the Sun is given by $T(r) = T_0 R^{-\delta}$, where $\delta = 0.467$. The three dimensional dust density distribution, $n_c(X, Y, Z)$, is composed of several structured components: a smooth cloud, three asteroidal dust bands and a circumsolar ring at 1AU. At a wavelength of 12 μm , the DIRBE satellite (Kelsall et al. 1998) measured the zodi components of the smooth cloud, dust bands and circumsolar ring as 28.476, 1.938, 3.324 MJy sr $^{-1}$ respectively. The simplified model adopted in this paper neglects the contribution to the zodi brightness of the dust bands and circumsolar ring.

Because of the relatively small inclination of the midplane of the smooth cloud distribution, the zodiacal light is the only component of the sky brightness that is not fixed on the celestial sphere. This important and unique feature, depicted in Figure 2, results in the temporal variation of zodi brightness observed in a given celestial direction by an Earth-based observer. The model calculations for a spacecraft are performed in heliocentric ecliptic coordinates (X, Y, Z) , where s, R_\oplus, λ represent respectively the height above the earth, the Earth-Sun distance (1 AU) and the heliocentric longitude of the earth.

$$X = R_\oplus \cos \lambda \quad (2)$$

$$Y = R_\oplus \sin \lambda \quad (3)$$

$$Z = s \quad (4)$$

The center of the smooth cloud is offset from the Sun by (X_0, Y_0, Z_0) and the resulting translated cloud coordinates are:

$$X' = X - X_0 \quad (5)$$

$$Y' = Y - Y_0 \quad (6)$$

$$Z' = Z - Z_0 \quad (7)$$

$$R_c = \sqrt{X'^2 + Y'^2 + Z'^2} \quad (8)$$

The vertical structure of the smooth dust cloud is determined by the height of its inclined symmetric midplane;

$$Z_c = X' \sin \Omega \sin i - Y' \cos \Omega \sin i + Z' \cos i \quad (9)$$

where i and Ω are the inclination and ascending node of the midplane.

The density of the smooth cloud is separable into radial and vertical terms;

$$n_c(X, Y, Z) = n_0 R_c^{-\alpha} f\left(\left|\frac{Z_c}{R_c}\right|\right), \quad (10)$$

where

$$f\left(\left|\frac{Z_c}{R_c}\right|\right) = \begin{cases} e^{-\beta\left(\frac{|Z_c/R_c|^2}{2\mu}\right)^r} & \text{for } \left|\frac{Z_c}{R_c}\right| < \mu \\ e^{-\beta(|Z_c/R_c|^2 - \mu/2)^r} & \text{for } \left|\frac{Z_c}{R_c}\right| \geq \mu \end{cases} \quad (11)$$

Following the same procedure of the DIRBE model, integration along the line of sight was performed from the satellite to an outer radial cutoff of 5.2 AU from the Sun. A particular line of sight is defined by two angles, the projected angle in the ecliptic plane and the angle from the ecliptic. To evaluate the zodi at a particular point along the orbit a single angle from the ecliptic (usually 30 degrees) was used and the zodi brightness was averaged over 360 degrees of the projected angle, these numbers were then normalized to go from 0 to 1. Our simulations found that the normalized zodi brightness were very close for angles above the ecliptic in the range of 0 to 60 degrees. Note that the spacecraft observes away from the ecliptic plane, so it rotates 180 degrees when it crosses the ecliptic.

3. Trajectories

3.1. The Equations of Motion

A vast amount of literature exists on the CR3BP (e.g. Gomez, Masdemont, & Simo 1998; Gomez et al. 1997; Howell 1997; Marchal 1990; Szebeheley 1967 and references therein). In almost all past research, the standard rotating coordinate system has been used with the origin set at the barycenter of the large primary, m_1 , and the small primary, m_2 . The x -axis is positive in the direction of m_1 , the z -axis is perpendicular to the plane of rotation and is positive when pointing upward, and the y -axis completes the set to yield a right-hand reference frame. Normalization is performed by setting $m_2 = \mu, m_1 = 1 - \mu$ where $\mu = m_2/(m_1 + m_2)$. Thus, m_1 is located at $(\mu, 0, 0)$ and m_2 is located at $(\mu - 1, 0, 0)$. Usually, this coordinate system is sufficient to model the problem and yields a fruitful characterization of diverse families of trajectories. However, in this study we have adopted a slightly different rotating coordinate system, which we found to be particularly useful for characterization of trajectories that reduce the zodi interference. The basic notion is to choose the origin of the coordinate system at the center of the small primary, Earth in our case — rather than the barycenter — and to normalize the masses by the mass of the large primary, the Sun in our case. This coordinate system was first used by Rabe (1961) and later by Breakwell (1963) in his approximate analysis of three-dimensional trajectories.

Following the usual analysis but in this variant coordinate system, let \mathbf{r} denote the position vector of the vehicle relative to Earth, and \mathbf{R} that of the earth relative to the Sun. The acceleration of the spacecraft relative to earth is given by Breakwell (1963):

$$\ddot{\mathbf{r}} = -\frac{\mu_E \mathbf{r}}{r^3} - \left[\frac{\mu_S (\mathbf{R} + \mathbf{r})}{|\mathbf{R} + \mathbf{r}|^3}, -\frac{\mu_S \mathbf{R}}{R^3} \right] \quad (12)$$

where μ_E is the gravitational constant of the earth and μ_S is the gravitational constant of the Sun.

The acceleration $\ddot{\mathbf{r}}$ is evaluated in a rotating Earth-fixed coordinate system as depicted in Figure 3. This local vertical reference frame originates at the center of the earth, with the x -axis directed radially outward along the local vertical, the y -axis lying along the direction of Earth's motion, and the z -axis normal to the ecliptic to complete the Cartesian right-hand setup.

We shall use the following unit convention: The position of the vehicle is measured in astronomical units (AU), where the mean Earth-Sun distance, assumed constant, is $|\mathbf{R}| = R = 1 \text{ AU} = 1.496 \times 10^8 \text{ km}$. The time unit is normalized by the earth's mean heliocentric angular velocity, i.e. $t = t^*/\sqrt{R^3/\mu_S}$ with t^* as the time measured in seconds. Accordingly, the velocity vector of the vehicle $\mathbf{v} = [\dot{x}, \dot{y}, \dot{z}]^T$ is normalized by $R/\sqrt{R^3/\mu_S}$. Also, let $\mu = \mu_E/\mu_S$.

The inertial frame used here, denoted by XYZ , is a heliocentric-ecliptic coordinate system, as depicted in Figure 3. By utilizing the above unit convention, the transformation from the rotating frame to the inertial frame can be found,

$$\begin{bmatrix} X \\ Y \\ Z \end{bmatrix} = \begin{bmatrix} \cos t & -\sin t & 0 \\ \sin t & \cos t & 0 \\ 0 & 0 & 1 \end{bmatrix} \begin{bmatrix} x+1 \\ y \\ z \end{bmatrix}. \quad (13)$$

Also, we define a pseudo-potential function,

$$\Omega(x, y, z) = \frac{1}{2}(x^2 + y^2) + \frac{\mu}{r} + \frac{1}{\rho} + x, \quad (14)$$

where

$$r = \sqrt{x^2 + y^2 + z^2} \quad (15)$$

is the distance from Earth, and

$$\rho = \sqrt{(x+1)^2 + y^2 + z^2} \quad (16)$$

is the distance from the Sun.

To proceed, we assume that the vehicle performs a ballistic motion, i.e., no control forces are used, and that the motion of the vehicle is unperturbed. Computing the well-known expression for the acceleration in a rotating coordinate frame yields the following equations of motion:

$$\ddot{x} - 2\dot{y} = \Omega_x \quad (17)$$

$$\ddot{y} + 2\dot{x} = \Omega_y \quad (18)$$

$$\ddot{z} = \Omega_z. \quad (19)$$

where the subscript stands for partial differentiation. Substituting from equation (14), equations (17)–(19) can be equivalently written as

$$\ddot{x} - x - 2\dot{y} = -\frac{\mu x}{(x^2 + y^2 + z^2)^{3/2}} - \frac{(1+x)}{[(x+1)^2 + y^2 + z^2]^{3/2}} + 1 \quad (20)$$

$$\ddot{y} - y + 2\dot{x} = -\frac{\mu y}{(x^2 + y^2 + z^2)^{3/2}} - \frac{y}{[(x+1)^2 + y^2 + z^2]^{3/2}} \quad (21)$$

$$\ddot{z} = -\frac{\mu z}{(x^2 + y^2 + z^2)^{3/2}} - \frac{z}{[(x+1)^2 + y^2 + z^2]^{3/2}} \quad (22)$$

or, in state-space vector form,

$$\dot{\mathbf{x}} = \mathbf{f}(\mathbf{x}), \quad (23)$$

where

$$\mathbf{x} \equiv [x, \dot{x}, y, \dot{y}, z, \dot{z}]^T. \quad (24)$$

Multiplying equations (20)–(22) by \dot{x} , \dot{y} , \dot{z} , respectively, adding the results and performing the integration, renders the integral of motion, the well-known Jacobi constant, given by:

$$C = \Omega(x, y, z) - \frac{1}{2}(\dot{x}^2 + \dot{y}^2 + \dot{z}^2). \quad (25)$$

Note that for any given initial conditions, the differential equations (20)–(22) are equivariant under the following transformations:

$$(x, y, z, t) \rightarrow (x, -y, z, -t) \quad \text{or} \quad (x, -y, -z, -t) \quad (26)$$

Hence, symmetries exist only for a backward integration of the equations of motion. However, various symmetries exist for different sets of initial conditions. An obvious symmetry that occurs in the xz plane is

$$x(t, (\mathbf{x}_0)_1) = x(t, (\mathbf{x}_0)_2), y(t, (\mathbf{x}_0)_1) = y(t, (\mathbf{x}_0)_2), z(t, (\mathbf{x}_0)_1) = -z(t, (\mathbf{x}_0)_2), \quad (27)$$

where

$$(\mathbf{x}_0)_1 = [x_0, \dot{x}_0, y_0, \dot{y}_0, z_0, \dot{z}_0]^T, (\mathbf{x}_0)_2 = [x_0, \dot{x}_0, y_0, \dot{y}_0, -z_0, -\dot{z}_0]^T. \quad (28)$$

Other symmetries that may exist as functions of initial conditions are much less obvious, due to the rotation of the coordinate system. The next section describes some stability considerations, which pave the way to synthesizing the constraints for the trajectory optimization procedure.

3.2. Practical Stability

One of the most important aspects of designing a trajectory is to define, study and characterize its stability. Since stability is a matter of definition, one has to use an appropriate stability framework that is suitable to the specific dynamical system involved. We have found that the so-called practical stability theory renders a good means to quantify our analysis and design of the CR3BP trajectories.

For given initial conditions, a trajectory is said to be practically stable if $r \leq \beta = r_{max}$ for $t \in [t_1, t_2]$, i.e., if the vehicle has not gone beyond some pre-specified distance from Earth at a given time interval. This stability definition is used to constrain the Genetic Algorithm optimization procedure (see §3.3 below). It reflects operational considerations, since at long distances from Earth communication becomes too costly.

Regions of practically stable motion for the spatial CR3BP can be semi-analytically determined by examining the curves of zero velocity, also known as Hill's regions. These curves are generated by plotting equipotential contours of the function (14), or, equivalently, plotting the position of the vehicle for different values of the Jacobi constant evaluated along $\dot{x} = \dot{y} = \dot{z} = 0$. The permissible regions of the vehicle's motion are confined by different values of C . For the three-dimensional case discussed here, sufficiency conditions for practically stable motion can be determined as follows (Szebehely 1967): Let $C(L_1, 0)$ denote the Jacobi constant for the Sun-Earth system evaluated along the zero velocity curve that intersects the Lagrangian equilibrium point L_1 . If

$$C > C(L_1, 0) = 1.0004513 \quad (29)$$

then the zones of possible motion of the vehicle are divided into three disconnected parts, either near the earth, near the Sun, or far away from both. The first two regions are practically stable and are known as Hill-stable regions (Marchal 1990). To distinguish between the practically stable regions and the third (not necessarily practically stable) region, we notice that the vehicle can drift away from the primaries only if the gradient of its potential function is positive. Hence, if equation (29) holds and in addition

$$\nabla\Omega(x, y, z) < 0 \tag{30}$$

a practically stable motion results.

Unfortunately, in order to satisfy both equations (29) and (30), one has to choose impractical initial conditions, since, generally speaking, orbits around the earth have a small normal motion magnitude, and trajectories that start near the Sun, which potentially have large normal deflections, can impose undesirable practical constraints on the mission. Instead, we look for different values of C that also result in practically stable trajectories (recall that the conditions above for stability are sufficient but not necessary). The basic requirement is to find initial conditions that lie within reasonable distance from Earth, but shift the vehicle to some (possibly) heliocentric orbit inclined to the ecliptic with the least possible energy. This task is fulfilled in the next section.

3.3. Optimal Trajectories

The discussion in the previous section stresses the complexity and counter-intuitive nature of solutions to the spatial CR3BP. We used a Genetic Algorithm (GA), specifically the Deterministic Crowding GA (Mahfoud 1995), to optimize the trajectories. This method is preferable over other optimization algorithms such as the gradient search and the simplex method because it avoids local minima (i.e. the search is performed over the entire state space) and promotes diversity of solutions.

We wish to maximize the normal displacement subject to the following

- the differential equations of motion;
- the practical stability constraint — the vehicle should not exceed a given distance from Earth during a given time interval;
- the initial position vector should lie outside Earth’s sphere but inside some pre-determined radius;
- the initial velocity vector should not exceed some pre-specified limit, derived from the overall propellant mass and capability of the launch vehicle.

See Gurfil & Kasdin (2001) for the GA parameters used for the trajectory optimizations. The trajectory search procedure is divided into two conceptual stages: characterization of optimal trajectories, where the search space is confined by rather loose bounds; and design, where the search space is narrowed in order to obtain practical results.

3.4. Trajectory Characterization

Eight optimization sets were carried out with different upper and lower bounds on the initial conditions and the maximum permissible distance from Earth (see Gurfil & Kasdin 2001). In order to visualize the

trajectories obtained, the individual with the highest fitness in the last generation is selected as the optimal solution. The time scale selected for visualization purposes is 15 years (larger than the 5 year time scale selected in the optimization itself).

The upper left panel in Figure 4 depicts the three-dimensional trajectory that resulted from the one of the optimization sets. Note that in this case the GA generated a quasiperiodic Lissajous trajectory that spirals above the ecliptic plane. In other words, if ω_z denotes the frequency of the vertical motion, and ω_x, ω_y denote characteristic frequencies of the radial and transverse motions, respectively, then this trajectory satisfies

$$\omega_z < \omega_x \approx \omega_y \quad (31)$$

which results in a large fraction of the orbit being above the ecliptic. Trajectories satisfying equation (31) are categorized as Type I trajectories. The main deficiency of Type I trajectories is their considerable distance from Earth. Note also that the solution depicted in the upper left panel of Figure 4 is asymmetric relative to the ecliptic plane, since most of the time the vehicle remains above the ecliptic. However, due to the symmetry property (27), a mirror image of the trajectory relative to the ecliptic can easily be generated. This is true for all the trajectories considered.

The upper right panel in Figure 4 depicts the three-dimensional trajectory that resulted from another optimization set. In this case the GA also generated a quasi-periodic Lissajous trajectory. However, here the trajectory satisfies⁵

$$\omega_z > \omega_x \approx \omega_y \quad (32)$$

which results in frequent vertical crossings of the ecliptic while maintaining reasonable distance from Earth. Trajectories satisfying equation (32) are categorized as Type II trajectories. The main deficiency of Type II trajectories is that frequent ecliptic crossing reduces the overall duration above a certain height. Note that as with Type I, the vertical crossing is asymmetric.

A third type of trajectory, shown in the lower left panel of Figure 4, was spotted when performing the characterization on yet a third optimization set. It satisfies the condition

$$\omega_z \approx \omega_x \approx \omega_y. \quad (33)$$

Thus, the trajectory is actually a quasi-periodic Lissajous trajectory as well, but it is almost closed in three dimensions, due to equation (33), as illustrated by the lower left panel of Figure 4.

A further examination shows that the other optimization sets produced Type I, II, and III trajectories as well. Generally speaking, reducing the practical stability limit reduces the frequency of the in-plane motion while keeping the frequency of the vertical motion almost unchanged. Reducing the initial velocity limit reduces the amplitude of both the vertical and the in-plane motion. The next step is to narrow the search space in order to design practical operational trajectories for space-borne observation missions. This step is carried out using GAs as well.

⁵ ω_x, ω_y in this case denote the frequencies of the dominant harmonics.

3.5. Trajectory Design: Low-Energy Optimal Trajectory

The design procedure is different from the characterization process, as the constraints of the problem are determined based upon practical engineering considerations. The major limitation of a real-life trajectory is the maximum energy available from the launcher for vehicle injection. We used twice the energy per unit mass required to inject a vehicle into an Earth departure hyperbola starting from a circular orbit of radius r_0 as our design constraint (this measure is known as C3).

To simplify the discussion, we shall describe only the first stage of the iterative design procedure. To this end, we chose to start from a 200 km parking orbit, i.e. $(r_0)_{max} = 6578$ km. Next, an estimate of the mass should be made. We chose the benchmark value 4000 kg, which is roughly the estimated mass of the current TPF configuration (Beichman et al. 1999). Using charts of lift capabilities versus C3 for various launchers, it was found that the Atlas ARS or the Delta IV could provide a C3 of approximately 40 given this mass. This C3 is smaller than the C3 required for generation of orbits normal to the ecliptic using planetary flybys (Buglia 1973) or direct injection (Renard 1970). Consequently, assuming $C3 = 40 \text{ km}^2/\text{s}^2$ and $(r_0)_{max} = 6578$ km, we have $(\nu_0)_{max} = 12.7 \text{ km/s}$. Also, we let $r_{max} = 2 \text{ AU}$.

Using the constraints mentioned, the GA was used to generate a population of optimal trajectories. The last generation of the GA optimization comprises several solutions, but two dominant solutions stand out (due to the symmetry property). Because the mid-plane of the zodiacal cloud is inclined 2.03 degrees to the ecliptic, with the ascending node at 77.7 degrees, going above the ecliptic renders slightly better reduction in zodi noise than going below the ecliptic, for the epoch used here. Hence, the initial conditions giving a positive normal displacement were chosen.

The optimization procedure will always pick ν_0 and C3 to lie on the constraint surface. Thus, properties of the low-energy optimal trajectories are as follows: $\nu_0 = 12.7 \text{ km/s}$, $C3=40 \text{ km}^2/\text{s}^2$ and accordingly $\Delta\nu = 4.9 \text{ km/s}$. The trajectory starts from a 200 km parking orbit. The maximum normal deflection above the ecliptic is 0.223 AU with a maximum distance of 2 AU from Earth. Although the resulting optimal trajectory is non-Keplerian, examining it in the inertial reference frame (13) reveals that it is a heliocentric orbit with the distance from the Sun satisfying $0.984 \leq \rho \leq 1.124$, assuming a mission lifetime of 5 years. This property is most important when considering solar arrays and power management for the mission, since it implies that modest-sized solar arrays can be used. Comparing the frequencies of the in-plane motion to the frequency of the normal motion classifies this trajectory as Type II.

Figure 5 depicts the normal, transverse, and radial displacements in the rotating Earth-fixed coordinate system, and the distance from Earth, for a 5 year mission for the low-energy optimal trajectory. The three-dimensional trajectory is presented as well. Because of the limited time scale, it seems as though the trajectory drifts away from Earth; however, the transverse and radial displacements are periodic having very slow frequencies relative to the frequency of the normal motion, hence a Type II trajectory results.

In order to estimate how much the proposed trajectory reduces the zodi noise, we used the zodi model described in §2 and incorporated it into the integration of the differential equations (20)–(22) using an appropriate coordinate transformation. First, note the periodic behavior resulting from the periodic normal displacement; in fact, these two variables are coherent. Second, note that for a positive normal displacement, the reduction in zodi brightness is 5% higher than for negative normal displacement. The maximum reduction in brightness is 67%. Averaging the values over time yields a mean reduction of 45%. Practically speaking, during 60% of the mission lifetime the zodi brightness is reduced by more than 50%. This allows for a considerable reduction in mirror size, permits faster data integration times and allows

collection of more observations for a given mission lifetime. Figure 7 shows a plot of the trajectory in heliocentric coordinates, where the intensity of the plot represents the normalized zodi brightness. Figure 8 is the cumulative brightness distribution for this trajectory. This represents the percentage of the mission life time for which the normalized zodi brightness is below a certain value.

Using the methodology proposed in Beichman et al. (1999) for the calculation of mirror diameter, we have found that for the TPF IR interferometer the noise decrease allows a reduction of 20% in mirror diameter, which yields up to 35% reduction in payload mass. Note that this reduction is not included in the optimization. Iteration on the optimization scheme would result in a reduced energy requirement for this reduced mass and perhaps a higher normal displacement.

3.6. Trajectory Design: High-Energy Optimal Trajectory

The previous section described an optimal trajectory that emerges from a 200 km parking orbit. The constraints $r_{max} \leq 2$ AU and $(\nu_0)_{max} = 12.7$ km/s resulted in a Type II trajectory that yielded a significant reduction in the zodi brightness. The purpose of this section is to present a different optimal trajectory which was obtained using other constraints. These constraints represent the maximum lift capability of existing launch vehicles and may even exceed them to some extent. Nevertheless, we have chosen to present this high-energy optimal trajectory because we believe that the energetic requirements for its implementation can be achieved by future launch vehicle such as the EELV or possibly via a combination of low-thrust electric propulsion and impulsive velocity changes. The principal merit of this trajectory is the outstanding reduction in zodi noise for most of the mission lifetime.

In this new trajectory, we have chosen to start from a 36,000 km Geosynchronous orbit (GEO), i.e. $(r_0)_{max} = 42,378$ km. Anticipating that the reduction in zodi noise allows the mass to be reduced by half⁶, we use a 2000 kg payload. With this mass, we chose $C3=95$ km²/s², which exceeds — but not by much — the lift capability of the Atlas ARS. This dictates the constraint $(\nu_0)_{max}$. Also, we let $r_{max} = 3$ AU. Again, the GA optimizer was used to synthesize an optimal trajectory.

Properties of the optimal trajectory are as follows: The trajectory starts from a 36,000 km orbit. The maximum normal deflection above the ecliptic is 0.374 AU with a maximum distance of 3 AU from Earth. As in the previous case, the resulting optimal trajectory drifts away from Earth for a given mission lifetime of 5 years. It is a non-Keplerian heliocentric orbit satisfying $0.958 \leq \rho \leq 2.274$. Comparing the frequencies of the in-plane motion to the frequency of the normal motion classifies this trajectory as Type III.

The optimal trajectory is visualized in Figure 9, which exhibits some of the extraordinary features of this trajectory. Figure 9 depicts the normal, transverse and radial displacements in the rotating Earth-fixed coordinate system, the 3D trajectory, and the distance from Earth, for a 5-year mission. Note that the minimum approach to Earth is 0.2 AU and is obtained after 802 days (approximately 2.2 years). The relatively close approach (0.2 AU) means that the orbit might be able to be perturbed to come close enough to Earth for replenishment or maintenance. Thus, this Type III trajectory offers somewhat of an advantage over the previously discussed optimal Type II trajectory. This specialized feature is typical of Type III trajectories.

⁶This is the maximum mass reduction possible for TPF. It is obtained when the zodi noise is completely eliminated. Other noise sources, however, prevent further mirror size and mass reduction (Beichman et al. 1999).

Similarly to the treatment in the previous section, we used the zodi model described in §2 to estimate the reduction in zodi brightness. Figure 10 describes the normalized zodi brightness as a function of time. The results are dramatic: the maximum reduction in brightness is 97%. Averaging the values over time yields a mean reduction of 75%. During 82% of the mission lifetime the zodi brightness is reduced by more than 70%. Figure 11 shows a plot of the trajectory in heliocentric coordinates, the intensity of the plot represents the normalized zodi brightness. Note that unlike in Figure 7, the zodi brightness is asymmetric; this is because one of the ecliptic crossings is farther away from the Sun than the other so the zodi brightness is lower. Figure 12 is the cumulative brightness distribution for this trajectory. This represents the percentage of the mission life time for which the normalized zodi brightness is below a certain value. The zodi reduction for this orbit allows for a considerable reduction in telescope mirror size, which not only results in a remarkable reduction in mass, but moreover, can significantly reduce the development and manufacturing costs.

Using the methodology proposed in Beichman et al. (1999) for the calculation of mirror diameter, we have found that for the TPF IR interferometer, the noise reduction due to the high-energy trajectory allows a reduction of 36% in mirror diameter, which yields up to 50% reduction in payload mass.

4. Summary and Discussion

The zodiacal dust is a significant problem for mid-IR missions like TPF because of its strong thermal emission. While this emission can be mitigated by a mission orbit at 5 AU from the Sun (as proposed by Landgraf & Jehn 2001), the associated design aspects renders such an orbit infeasible even though the zodi is considerably reduced. For a finite mission lifetime, the overall scientific return is dramatically reduced due to the time required to get to a 5AU orbit. Moreover, these trajectories require very large solar arrays and massive communication antennas. Also, in case of a failure, it is practically impossible to replace the damaged components or to perform other replenishment missions. Note also that going a unit distance above the ecliptic decreases the zodi intensity considerably more than going a unit distance from the Sun within the ecliptic. This was the motivation for the study of out-of-the-ecliptic trajectories for space-borne observatories. The spacecraft observes away from the ecliptic plane, so that it turns over when it crosses the ecliptic plane. We have used genetic algorithms as the parameter optimization procedure which has resulted in a fruitful probing of the complex dynamics of the restricted problem. For example, the farthest either of our trajectories goes from Earth is 2.2 AU within a 5 year mission lifetime, which means an order of magnitude smaller solar arrays can be used than for a mission at 5 AU. Also, data collection and scientific interpretation can begin right away instead of having to wait several years. A direct trip to 5 AU requires a C3 of $80 \text{ km}^2/\text{s}^2$ (Meissinger, Wertz, & Dawson 1997), equivalent to our high energy trajectory, and a travel time of two years. Galileo's trajectory used a C3 of $13 \text{ km}^2/\text{s}^2$ (Meissinger et al.), but it took 6 years to reach Jupiter, with most of that time spent around 1 AU, and required correct planetary alignment to allow for three planetary flybys. Going to 5 AU also means long travel times through the ecliptic plane, which increases the chance of micrometeorite damage. Finally, we did not iterate on mass reduction in our optimization procedure. The large mass reduction would provide a reduction in launch costs or alternatively an orbit with a greater normal displacement above the ecliptic.

Three types of out-of-ecliptic trajectories were identified using Deterministic Crowding GAs. Type I was characterized by a high frequency in-plane motion and a slow frequency normal displacement. This type was obtained for large departures from Earth ($> 5\text{AU}$). Type II was obtained when the maximal Earth-departure was restricted to small values ($< 2 \text{ AU}$). Its main feature was low frequency in-plane

motion and high frequency out-of-the-plane motion. Type III was obtained for an intermediate Earth departure distance (3 AU) and exhibited almost equal characteristic frequencies. This classification was used as the infrastructure for design of optimal trajectories. It should be stressed that Type II trajectories can also achieve large normal displacements if an appropriate C3 is chosen. (Recall that C3 is twice the energy per unit mass which is required to inject a vehicle into an Earth departure hyperbola starting from a circular orbit of radius r_0 .) However, Type III trajectories offer both longer times above the ecliptic and a closer approach to Earth than the other two types of trajectories. Type II trajectories provide a smaller departure from Earth and a shorter distance from the Sun. These facts should be traded off when considering utilization of either of these trajectories for real-life space-borne observation missions. The trajectories are selected *a priori* to be stable; hence, stationkeeping maneuvers are reduced to correcting perturbations only, and, furthermore, escape to an undesirable region is impossible.

The design process incorporated tighter parameter constraints than the characterization procedure. In order to obtain a Type II optimal trajectory, an estimate of the payload mass was made and an appropriate C3 was chosen, based upon lift capabilities of existing launchers. We call this the low-energy trajectory. The second optimal trajectory was a high-energy trajectory. Although its required C3 exceeded the capabilities of existing launchers, it might constitute a worthwhile alternative using future launchers or a combination of impulsive and electric propulsion. The two trajectories have the properties described in Table 1.

The most important point is that both trajectories imply that the overall collecting area and hence the mass and cost can be significantly reduced. This is due to the substantial reduction in zodi which results from the out-of-the-ecliptic displacement of 0.22 and 0.37 AU for the low and high energy trajectories respectively. For comparison, in typical libration point trajectories, the normal excursion is up to an order of magnitude smaller. This high displacement also considerably reduces the probability of micrometeorite or space debris damage, which could extend the mission lifetime. The low energy trajectory has a mean distance of 1 AU from the Sun which guarantees that standard solar arrays can be used for power supply. The high-energy trajectory, on the other hand, could require larger solar arrays, though still well within current capabilities with minimal increase in the mass. The drift from Earth is 2 AU for the low energy trajectory and so communication and uplink/downlink operations can be carried out using modest-sized antennas. The high energy trajectory has a drift from Earth of 3 AU and larger antennas would be required. Although the high-energy trajectory requires more communication and operating power, and relies on future planned launch vehicles, the expected reduction in mass, development and manufacturing costs is likely to be large and should compensate for the expected increase in launch costs.

The mass reduction figures used in this design process are rather specific for a TPF mid-IR interferometer looking for terrestrial planets. As the local zodi cloud noise is mitigated, a noise floor is reached. This minimum noise level has specific characteristics derived from the mission itself, and is determined by other noise sources that become drivers as we escape the ecliptic. If the trajectories obtained are generalized to other missions, such as filled aperture telescopes like NGST and SIRTF, even further benefits in terms of mass reduction are possible. Benefits are not as dramatic for optical missions because the zodi intensity is lower in the visible wavelength region.

The quest for optimal trajectories for space-borne observatories has by no means been exhausted by this study. While the foundation for out-of-the-ecliptic trajectories has been built, there are several additional points that need to be clarified and further investigated. These include optimal transfers from Earth to the initial orbit, use of electric propulsion, searching for optimal initial conditions in other regions of state space, including perturbations from other solar system bodies, and using lunar and planetary flybys.

This work was performed as part of the Ball Aerospace architecture studies for the Terrestrial Planet Finder mission under JPL contract 1217281. The authors gratefully acknowledge the help and support of the people at Ball and JPL as well as the other members of the science team and the Princeton Terrestrial Planet Finder group. SS is supported by the W.M. Keck Foundation.

REFERENCES

- Beichman, C. A., Woolf, N. J., & Lindensmith 1999 The Terrestrial Planet Finder (TPF), NASA/JPL Publication 99-3, May 1999.
- Breakwell, J. V. 1963, Trajectories Launched Normal to the Ecliptic, in Proceedings of the 14th International Astronautical Congress, aris, p. 128
- Buglia, J. J. 1973, Journal of Spacecraft and Rockets, 10, 601
- Gomez, G., Masdemont, J., & Simo, C., 1998, Journal of the Astronautical Sciences, 46, 135
- Gomez, G., Massdemont, J., & Simo, C. 1997, Advances in the Astronautical Sciences, 95, 117
- Goudas, C. L. 1963, Icarus, 2, 1
- Gurfil, P., & Kasdin, J 2001, submitted to the Journal of Astronautical Sciences
- Henon, M. 1974, A&A, 30, 317
- Howell, K. C., Barden, B. T., & Lo., M. W., 1997, Journal of the Astronautical Sciences, 45, 161
- Kelsall, T., Weiland, J. L., Franz, B. A., Reach, W. T., Arendt, R. G., Dwek, E., Freudenreich, H. T., Hauser, M. G., Moseley, S. H., Odegard, N. P., Silverberg, R. F., & Wright, E. L. 1998 ApJ, 508, 44
- Landgraf, M. & Jehn, R. 2001, Ap&SS, in press, astro-ph/0103005
- Lubow, S. 2000, <http://icarus.stsci.edu/~lubow/ngst/orbits.html>
- Mahfoud, S. W. 1995, Niching Methods for Genetic Algorithms, Illinois Genetic Algorithms Laboratory Report No. 95001, University of Illinois at Urbana-Champaign
- Marchal, C. 1990, The Three-Body Problem (New York: Elsevier)
- Meissinger, H., Wertz, J., & Dawson, S. 1997, AAS/AIAA Astrodynamics Specialist Conference, <http://www.smad.com/analysis/hmeissinger.pdf>
- Rabe, E. 1961, ApJ, 66, 500
- Renard, M. L. 1970, Journal of Spacecraft and Rockets, 7, 1208
- Szebehely, V. 1967, Theory of Orbits, (New York: Academic Press)

Table 1: Properties of the optimal trajectories

	Low-energy trajectory	High-energy trajectory
Max. displacement above ecliptic	0.223 AU	0.374 AU
Max. zodi reduction	67%	97%
Fraction of mission/reduction in brightness	60%/50%	82%/70%
Mirror diameter reduction	20%	35%
Mass reduction	$\lesssim 35\%$	$\lesssim 50\%$
Mean distance from Sun	1 AU	1.6 AU
Drift from Earth	2 AU	3 AU

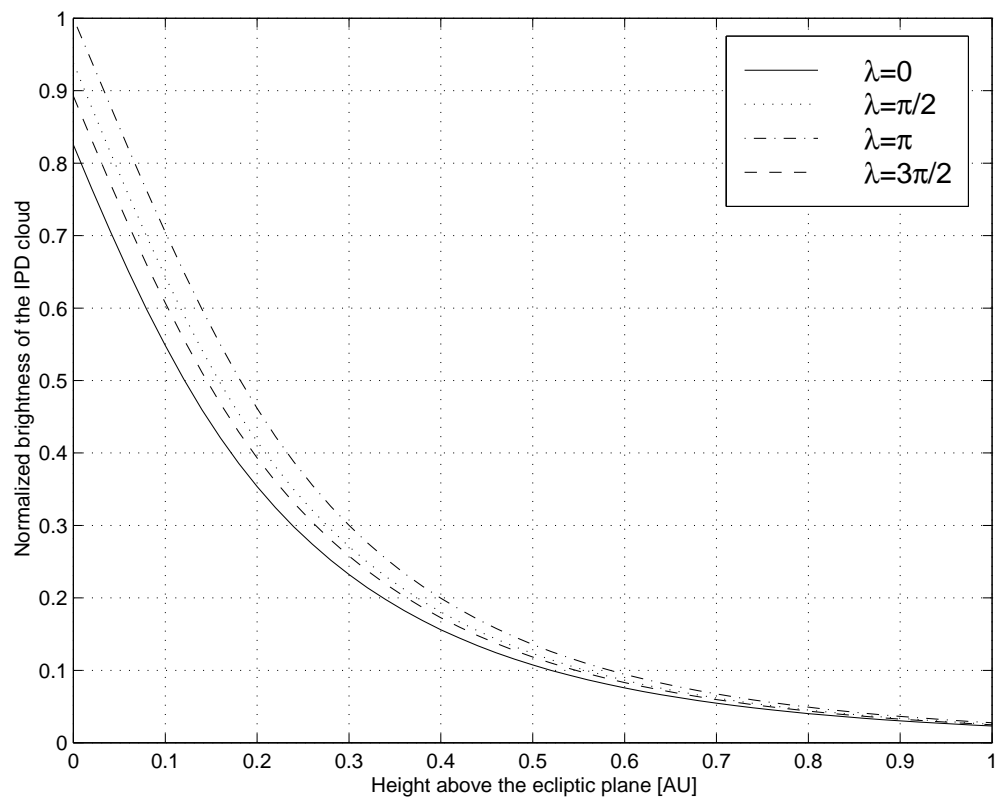


Fig. 1.— Variation of the brightness of the local interplanetary dust cloud (thermal emission only) as viewed from Earth along the line-of-sight normal to the ecliptic plane at four different Earth positions.

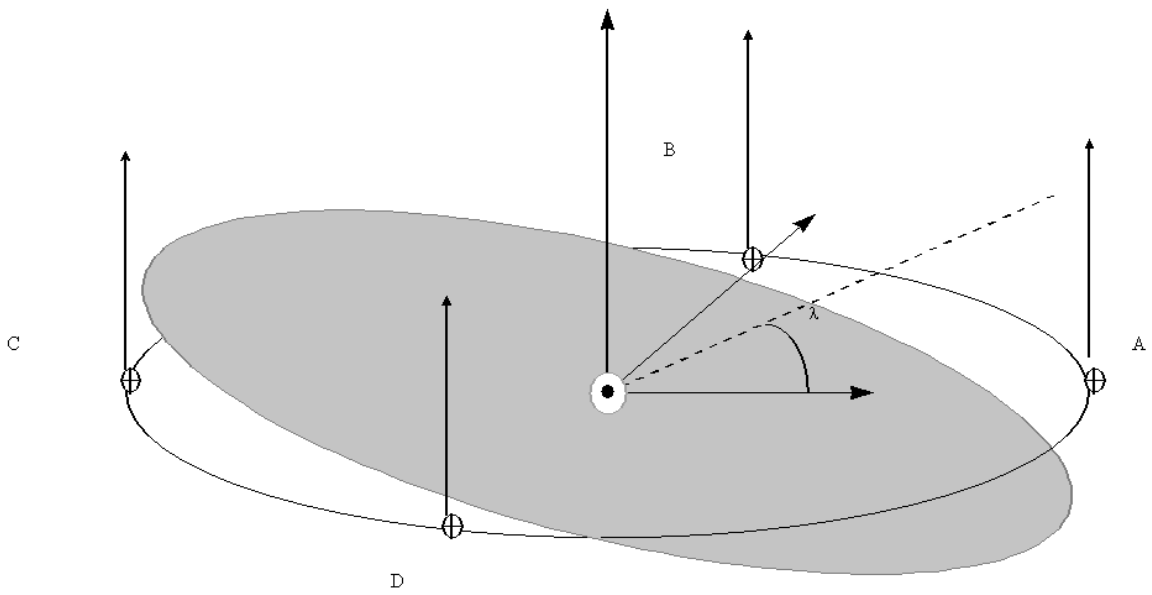


Fig. 2.— Inclination of the symmetric zodiacal dust cloud with respect to the Sun-Earth ecliptic plane. A, B, C, and D correspond to the positions of the line-of-sights ($\lambda = 0, \pi/2, \pi, 3\pi/2$) shown in Figure 1.

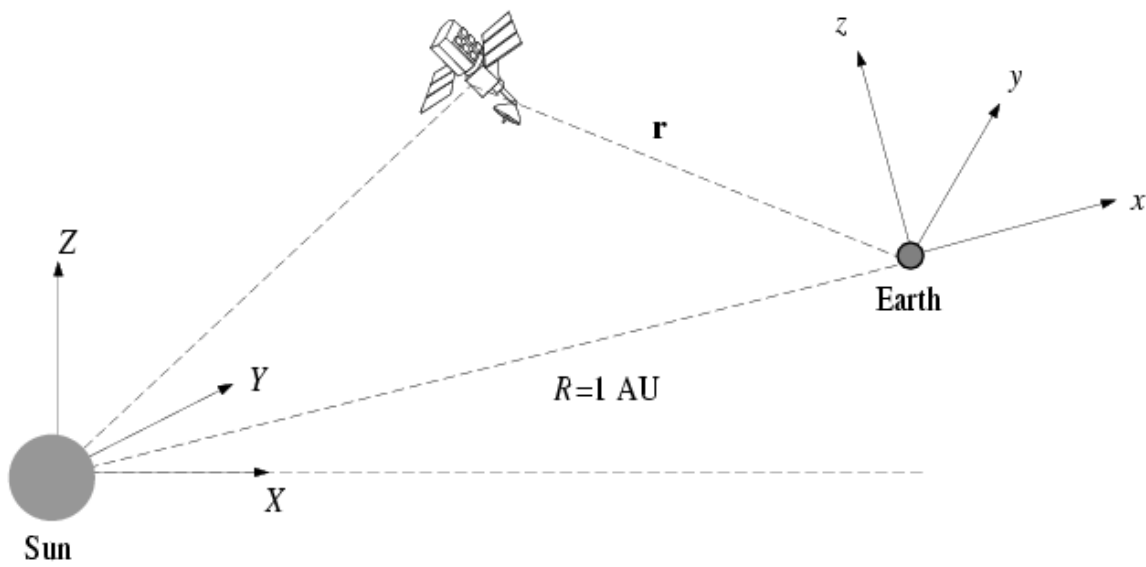


Fig. 3.— Definition of the coordinate systems.

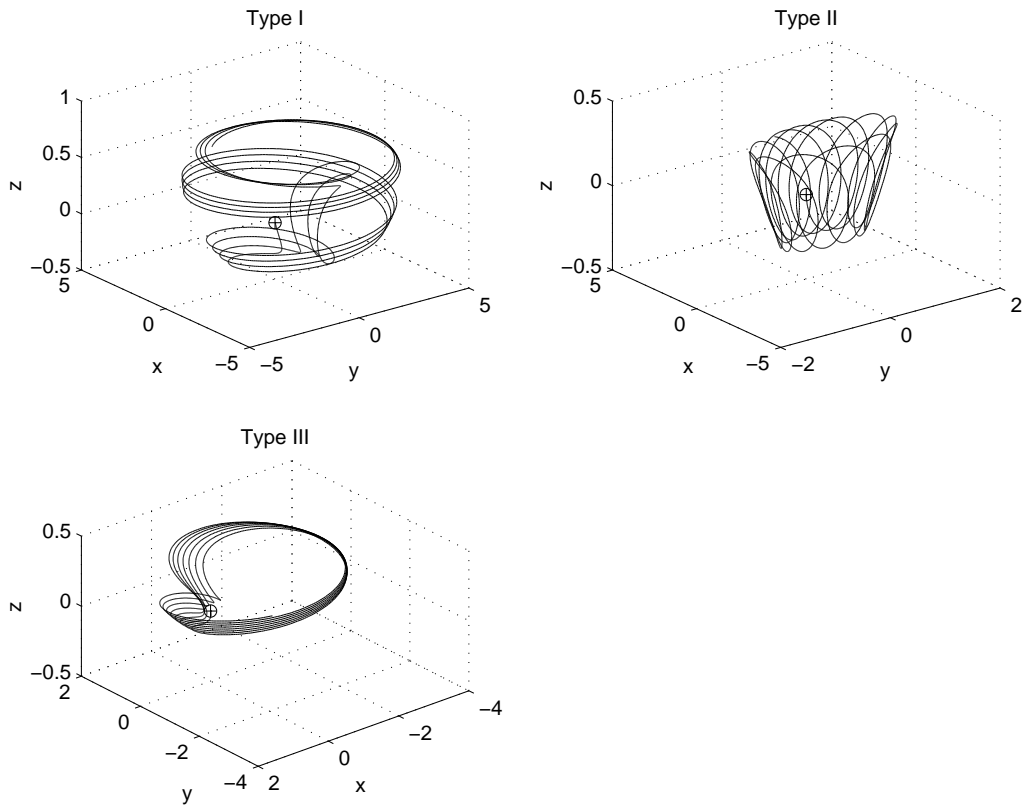


Fig. 4.— Type I, II, and III trajectories resulting from the characterization process shown in an Earth-fixed rotating coordinate system.

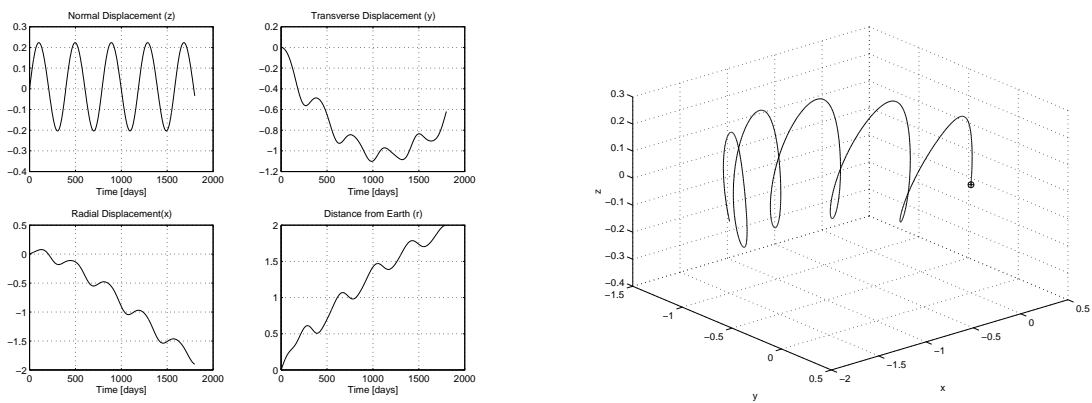


Fig. 5.— Time histories of the displacement components, the 3D trajectory and the distance from Earth for the low-energy optimal trajectory.

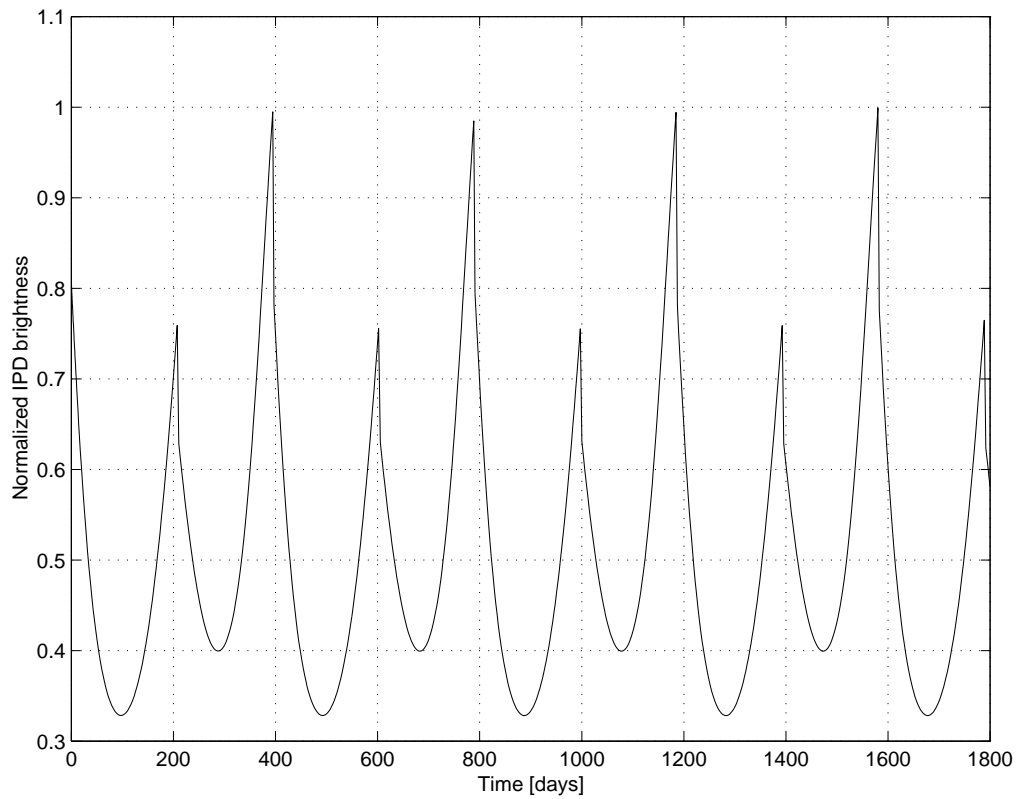


Fig. 6.— The time history of the normalized zodiacal dust brightness along the low-energy optimal trajectory shows that the maximum reduction in brightness is 67%. Note that the spacecraft would observe the sky away from the ecliptic plane; when the spacecraft crosses the ecliptic plane it would turn over.

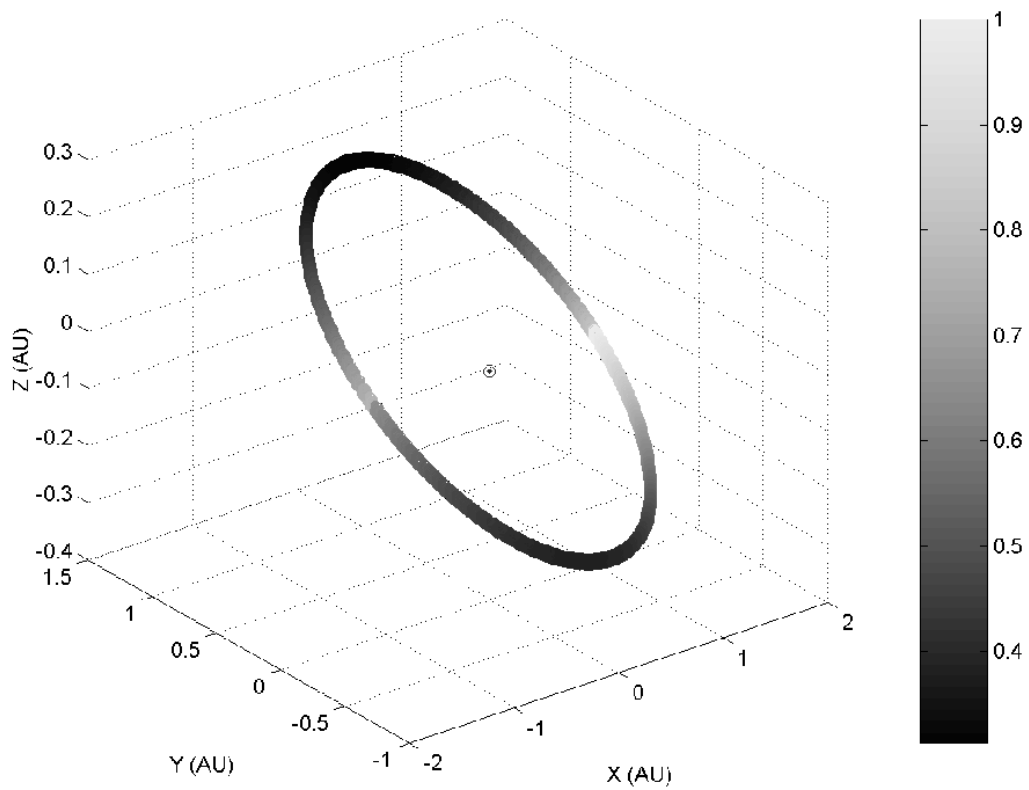


Fig. 7.— Normalized average zodi brightness for the high energy trajectory. The trajectory is shown in heliocentric coordinates with the position of the Sun indicated by “ \odot ”.

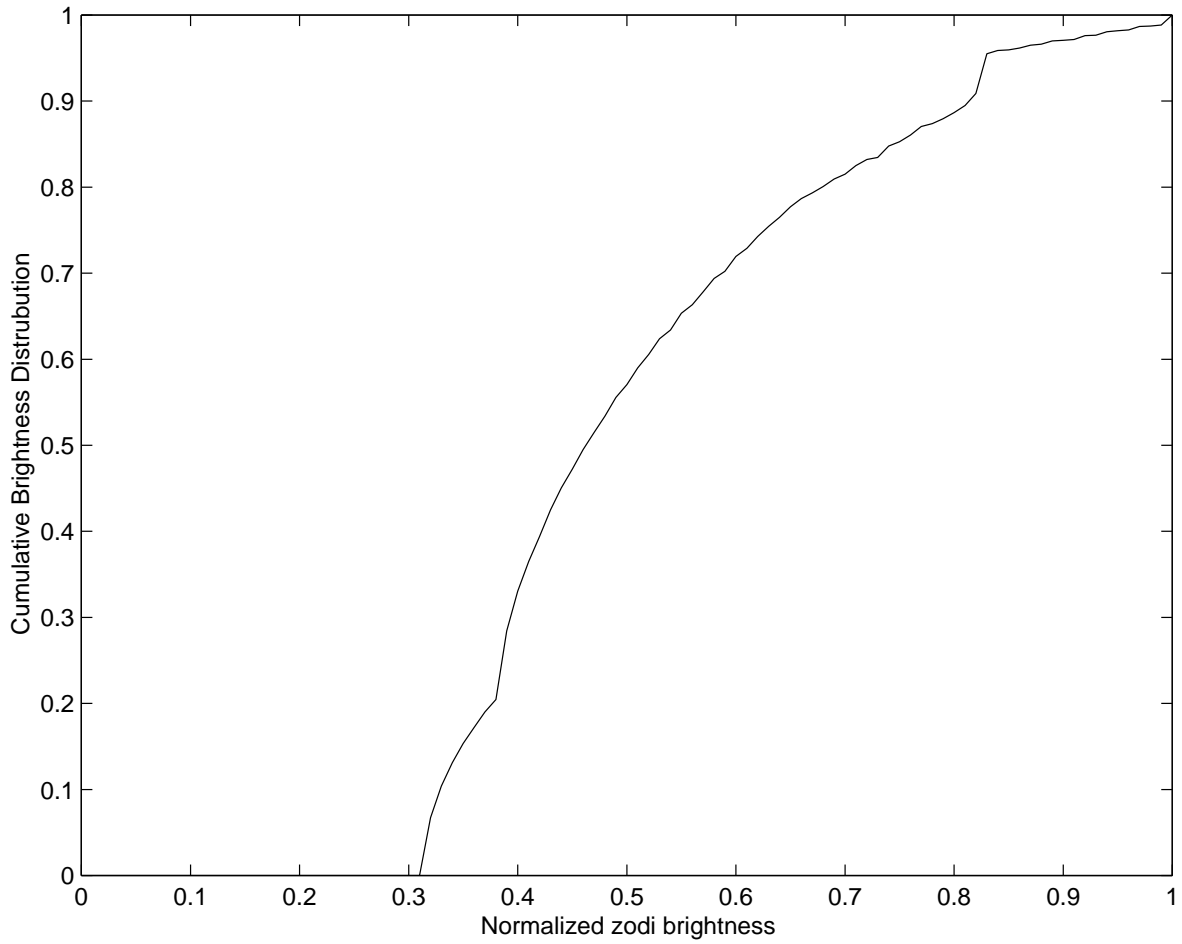


Fig. 8.— Cumulative brightness distribution for the low energy orbit.

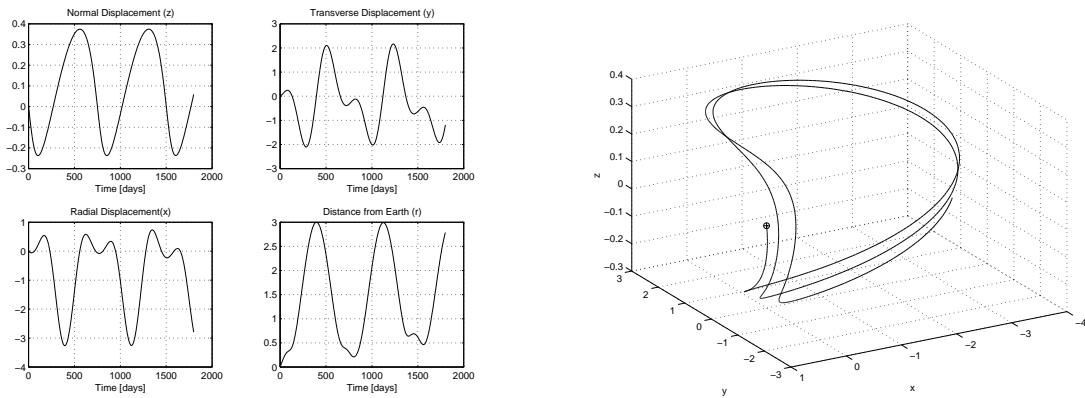


Fig. 9.— Time histories of the displacement components, the 3D trajectory and the distance from Earth for the high-energy optimal trajectory.

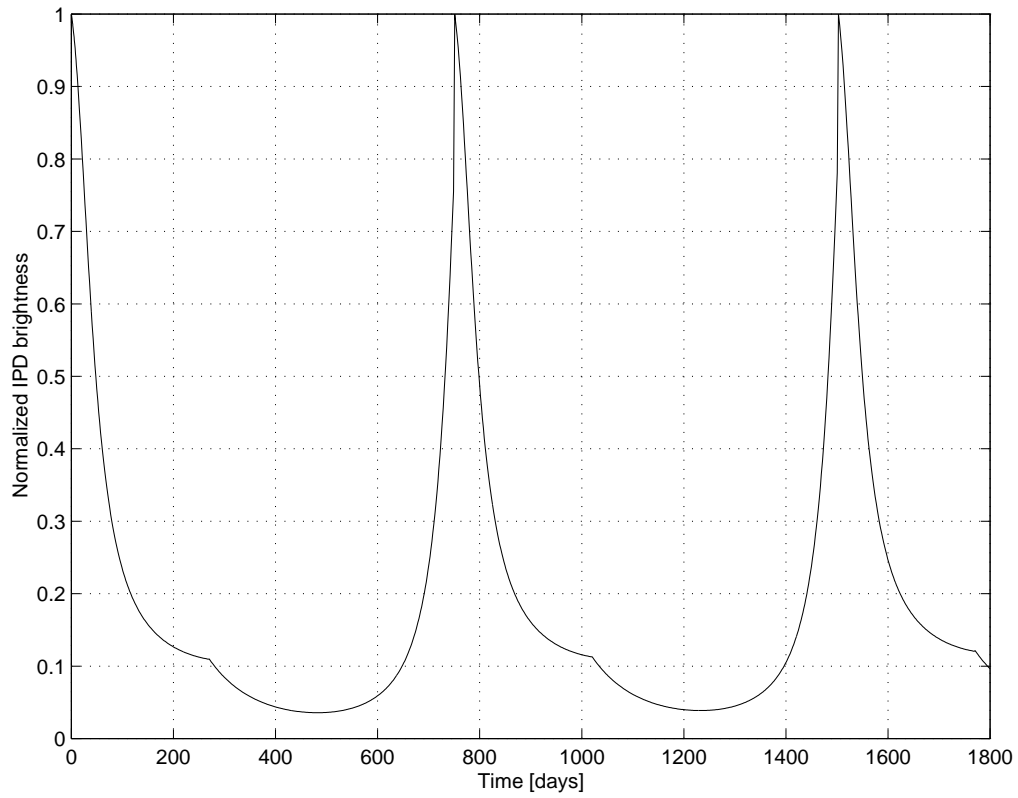


Fig. 10.— The time history of the normalized zodi brightness along the high-energy optimal trajectory shows a dramatic maximum reduction of 97% in brightness. During 82% of the mission lifetime, the zodi brightness is reduced by more than 70%. Note that the spacecraft would observe the sky away from the ecliptic plane; when the spacecraft crosses the ecliptic plane it would turn over.

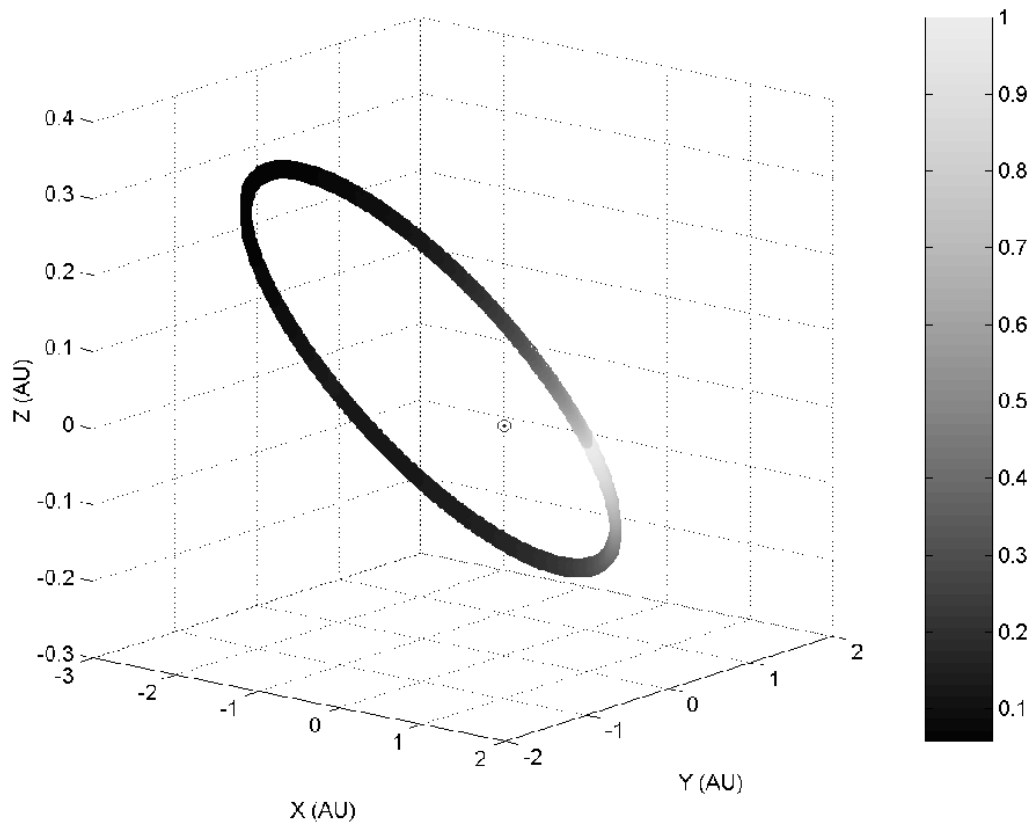


Fig. 11.— Normalized average zodi brightness for the high energy trajectory. The trajectory is shown in heliocentric coordinates with the position of the Sun indicated by “ \odot ”.

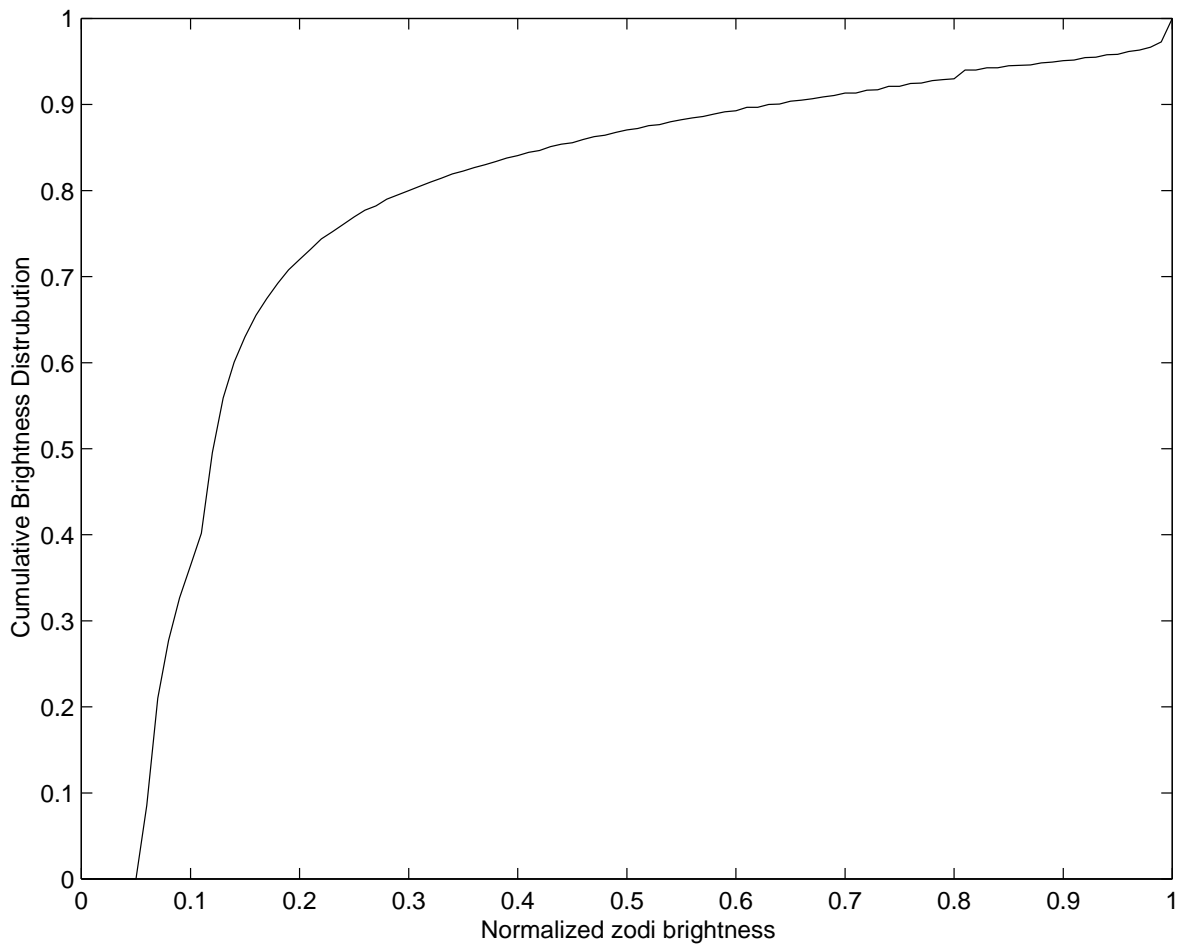


Fig. 12.— Cumulative brightness distribution for the high energy orbit.